

# Tunable Catalytic Alloying Eliminates Stacking Faults in Compound Semiconductor Nanowires

Hoseok Heo,<sup>‡,⊥</sup> Kibum Kang,<sup>‡,⊥</sup> Donghun Lee,<sup>‡</sup> Li-Hua Jin,<sup>§</sup> Hyeon-Jun Back,<sup>||</sup> Inchan Hwang,<sup>‡</sup> Miseong Kim,<sup>‡</sup> Hyun-Seung Lee,<sup>‡</sup> Byeong-Joo Lee,<sup>‡</sup> Gyu-Chul Yi,<sup>||</sup> Yong-Hoon Cho,<sup>§</sup> and Moon-Ho Jo<sup>\*,‡,‡</sup>

<sup>‡</sup>Department of Materials Science and Engineering and <sup>‡</sup>Division of Advanced Materials Science Science (WCU), Pohang University of Science and Technology (POSTECH), San 31, Hyoja-Dong, Nam Gu, Pohang, Gyungbuk 790-784, Korea

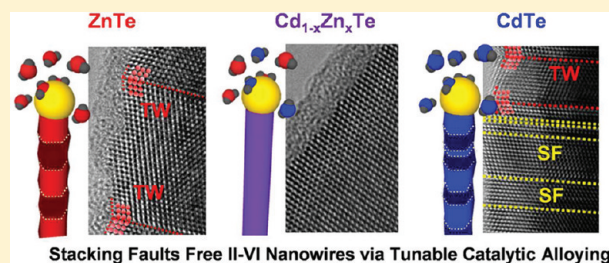
<sup>§</sup>Department of Physics and Graduate School of Nanoscience & Technology (WCU), Korea Advanced Institute of Science and Technology (KAIST), Daejeon 305-701, Korea

<sup>||</sup>National Creative Research Initiative Center for Semiconductor Nanorods and Department of Physics and Astronomy, Seoul National University, Seoul 151-747, Korea

## S Supporting Information

**ABSTRACT:** Planar defects in compound (III–V and II–VI) semiconductor nanowires (NWs), such as twin and stacking faults, are universally formed during the catalytic NW growth, and they detrimentally act as static disorders against coherent electron transport and light emissions. Here we report a simple synthetic route for planar-defect free II–VI NWs by tunable alloying, i.e.  $\text{Cd}_{1-x}\text{Zn}_x\text{Te}$  NWs ( $0 \leq x \leq 1$ ). It is discovered that the eutectic alloying of Cd and Zn in Au catalysts immediately alleviates interfacial instability during the catalytic growth by the surface energy minimization and forms homogeneous zinc blende crystals as opposed to unwanted zinc blende/wurtzite mixtures. As a direct consequence of the tunable alloying, we demonstrated that intrinsic energy band gap modulation in  $\text{Cd}_{1-x}\text{Zn}_x\text{Te}$  NWs can exploit the tunable spectral and temporal responses in light detection and emission in the full visible range.

**KEYWORDS:** Twin defects, stacking faults, II–VI semiconductor, band-gap modulation



It is notorious that planar defects are universally formed during the catalytic growth of compound semiconductor nanowires (NWs), due to the interfacial instability,<sup>1,2</sup> and the consequential defect states within the energy gaps limit coherent electron transport and optical band transitions,<sup>3–5</sup> unless they are deterministically controlled in periodicity to form sub-bands in superlattice structures.<sup>6–11</sup> In their bulk phase, many types of III–V and II–VI compound semiconductors are stabilized as the zinc blende (ZB) crystal structure. However, in the catalytic growth of such semiconductor NWs, the rotational twins and defects are persistently present, forming the mixture of the cubic ZB and the hexagonal wurtzite (WZ) crystal structures within the individual NWs. This phenomenon has been extensively investigated by both various growth methods and thermodynamic calculations;<sup>12–19</sup> however, the systematic control for the growth of the single crystallographic NW phase of one kind over the other is not readily available to date. Here we report a simple synthetic route for the planar-defect-free II–VI NWs via tunable alloying, i.e., single ZB phase  $\text{Cd}_{1-x}\text{Zn}_x\text{Te}$  NWs ( $0 \leq x \leq 1$ ). It was found that the eutectic alloying of Cd and Zn in Au catalysts immediately alleviates the interfacial instability during the catalytic growth and forms homogeneous ZB crystals as

opposed to unwanted ZB/WZ mixtures. Thereby we have achieved the growth of ZB single-crystalline phase  $\text{Cd}_{1-x}\text{Zn}_x\text{Te}$  NWs, whose relative composition, and thus the energy band gap, is controllably tuned over the entire alloying range. We then demonstrated that the spectral and temporal responses in photodetection and photoluminescence fully exploit the intrinsic energy band gap modulation in the visible range with the absence of the previously known defect states.

$\text{Cd}_{1-x}\text{Zn}_x\text{Te}$  ( $0 \leq x \leq 1$ ) alloy NWs in our study were synthesized by the Au catalyst-assisted vapor deposition from solid powder precursors. High-purity CdTe (99.999%, Alfa Aesar) and ZnTe (99.99%, Alfa Aesar) powders were separately placed in alumina boats and were loaded inside a 12-in. hot-walled quartz-tube furnace. The ZnTe powders were located in the central heating zone of a quartz tube, and the CdTe powders were located at the 4 cm upstream away from the tube center because the vapor pressure of CdTe is much higher than that of ZnTe.  $\text{SiO}_2/\text{Si}$  wafers (15 mm  $\times$  15 mm) as the growth substrates, on which a 2 nm thick Au film was deposited by

**Received:** November 6, 2011

**Revised:** December 27, 2011

**Published:** January 23, 2012

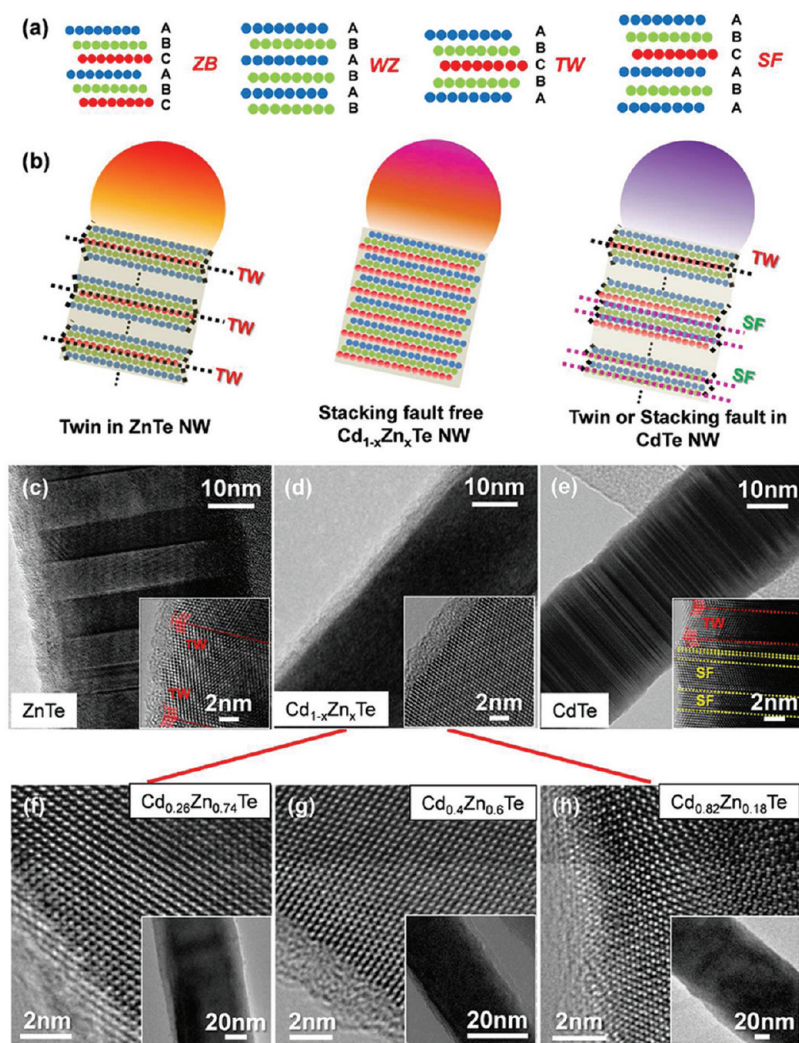


**Figure 1.** (a) The layer stacking sequences in the zinc blende structure and wurtzite structure. Twins and stacking faults are formed in the interim of such stacking sequences. Different layer colors denote the atomic stacking sequence from the  $\langle 110 \rangle$  zone axis. (b) Schematics of the layer stacking sequences observed from ZnTe,  $\text{Cd}_{1-x}\text{Zn}_x\text{Te}$  ( $0 < x < 1$ ), and CdTe NWs in our study. (c, d, e) Representative TEM images of an individual ZnTe,  $\text{Cd}_{1-x}\text{Zn}_x\text{Te}$  ( $0 < x < 1$ ), CdTe NW. The insets show the detailed planar-defect structures, such as stacking fault in yellow dashed lines and twin in red. (f, g, h) Representative high-resolution TEM images of  $\text{Cd}_{1-x}\text{Zn}_x\text{Te}$  ( $0 < x < 1$ ) NWs with three different Zn composition: (f)  $x = 0.74$ , (g)  $x = 0.6$ , and (h)  $x = 0.18$ . The insets are TEM images at the lower magnifications.

thermal evaporation, were placed at the 12 cm downstream from the tube center. Prior to heating, the quartz furnace was evacuated to  $10^{-3}$  Torr and was purged with the high-purity nitrogen ( $\text{N}_2$ ) to eliminate residual oxygen. When the center of furnace was heated to  $700^\circ\text{C}$ , the local temperatures within the tube are measured to be  $700^\circ\text{C}$  at the ZnTe powder boat,  $650^\circ\text{C}$  at the CdTe powder boat, and  $500^\circ\text{C}$  at the growth substrates, respectively. During the preheating and the growth, the 400 sccm of nitrogen ( $\text{N}_2$ ) and the 200 sccm of hydrogen ( $\text{H}_2$ ) were introduced as a carrier gas at the total pressure of 100 Torr. The full composition of  $\text{Cd}_{1-x}\text{Zn}_x\text{Te}$  ( $0 \leq x \leq 1$ ) NWs is modulated by the relative molar ratio of CdTe and ZnTe powders by changing the relative amount of powders from 0 to 100 mg. Pure CdTe and ZnTe NWs were synthesized by the same process solely using CdTe and ZnTe powder precursors.

The crystal structure of ZnTe,  $\text{Cd}_{1-x}\text{Zn}_x\text{Te}$ , and CdTe NWs was characterized by a high-resolution transmission electron microscope (HRTEM), with the particular focus on the planar defects along the NW axis. Typically, as in Figure 1c,e, the pure

ZnTe and CdTe NWs possess the ZB/WZ mixed crystal textures with the periodic stacking faults and twin defects (red dashed line: twin; yellow dashed line: stacking fault); see also Figure 1a. Therein each polytypism was carefully identified with the TEM diffractions, as further specified in Figure S1. Most of all, it is remarkable that the  $\text{Cd}_{1-x}\text{Zn}_x\text{Te}$  alloy NWs show single-crystalline ZB structures, where either twins or stacking faults are completely absent, as shown in Figure 1d. We emphasize that this planar-defect free structure was commonly observed over the entire alloying compositions at which we have examined over the 20 samples, as represented in Figure 1f–h. For example, we confirm that the alloy NWs, such as  $\text{Cd}_{0.26}\text{Zn}_{0.74}\text{Te}$ ,  $\text{Cd}_{0.4}\text{Zn}_{0.6}\text{Te}$ , and  $\text{Cd}_{0.82}\text{Zn}_{0.18}\text{Te}$  NWs, maintain the single-crystalline ZB texture. This observation clearly demonstrates that the catalytic Cd:Zn alloying immediately prevents the formation of stacking faults and twin defects, which are otherwise commonly present in parent ZnTe and CdTe NWs. We schematically illustrate such phenomena in Figure 1b. We have further synthesized the  $\text{Cd}_{1-x}\text{Zn}_x\text{Te}$  alloy NWs over the full composition range, as evidently characterized

with the X-ray diffraction scans in Figure 2 (see also Supporting Information Figure S2). It shows that the (111) diffraction peak

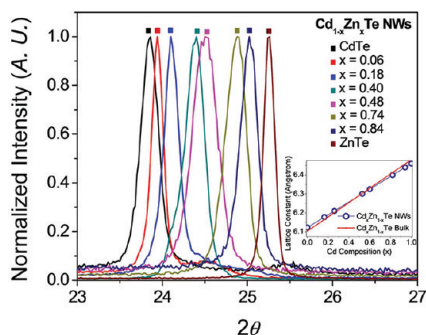


**Figure 2.** X-ray diffraction (XRD)  $\theta$ - $2\theta$  scans of  $\text{Cd}_{1-x}\text{Zn}_x\text{Te}$  ( $0 \leq x \leq 1$ ) NWs. The peaks are the (111) diffraction of the zinc blende structure and progressively shift between those of CdTe and ZnTe NWs. (The full widths at half-maximum in each peak are  $0.075^\circ$ ,  $0.125^\circ$ ,  $0.150^\circ$ ,  $0.200^\circ$ ,  $0.130^\circ$ , and  $0.105^\circ$ , respectively.) The inset shows the variation in lattice constants as a function of Cd composition, extracted from the (111) diffractions.

of  $\text{Cd}_{1-x}\text{Zn}_x\text{Te}$  NWs progressively shifts to the lower angles from that of CdTe NWs to that of ZnTe NWs with increasing Zn content. The variation in lattice constant is summarized in the inset, and it follows the general trend of the bulk  $\text{Cd}_{1-x}\text{Zn}_x\text{Te}$  crystals in Vegard limit.<sup>20</sup>

The ZB/WZ mixture crystallization in the catalytic III-V and II-VI semiconductor NWs has been extensively investigated for its origin both by various empirical observations and thermodynamic/kinetic calculations.<sup>6,21-23</sup> Typically, within the framework of the nucleation kinetics model during the catalytic growth at the vapor (V)-liquid (L)-solid (S) phase boundary, it was suggested that the nucleation energy barrier of WZ and ZB phases is largely dependent on two thermodynamic parameters: (1) the supersaturation at the L-S boundary,  $\Delta\mu_{L-S}$ , and (2) the surface energy changes at the phase boundaries.<sup>6,21-23</sup> Therein, the ratio of the nucleation energy barriers ( $\Delta G_{WZ}/\Delta G_{ZB}$ ) for ZB ( $\Delta G_{ZB}$ ) and WZ ( $\Delta G_{WZ}$ ) NWs, which determines the predominant crystal phase, is proportional to the combination of "the supersaturation ratio term between ZB and WZ" and "the surface energy ratio term between ZB and WZ".<sup>21-23</sup> Notably, the interfacial instability, arising from a strong competition ( $\Delta G_{WZ}/\Delta G_{ZB} \cong 1$ ) between the ZB and WZ, is responsible for the mixture formation. Algra et al.<sup>6</sup> showed that the increasing dopant (Zn) incorporation into InP NW catalysts lowers the free energy ratio between WZ and ZB InP NWs, which is preferable for the low-energy ZB phase, and thus promotes a larger ZB segment formation over the WZ segments along the NW axis. Furthermore, Wallein et al.<sup>22</sup> observed the decreased NW diameters at the longer ZB segment over the WZ segments within individual NWs upon increasing Zn dopants, accompanied by an increase in contact angles of catalysts, from which they also interpreted as that the total surface energy change favors the ZB crystallization. The fact that we observed the single-crystalline ZB phase in the alloy NWs, instead of the modulation in the relative portion of WZ/ZB mixtures, indicates that the delicate balance between the WZ and ZB phase formation is significantly tipped off during the catalytic alloy crystallization. We first consider a possible origin by examining the  $\Delta\mu_{L-S}$ , which can be indirectly traced by the amount of the residual element within the catalysts.

Figure 3a shows such an elemental analysis, done on the individual catalysts of various  $\text{Cd}_{1-x}\text{Zn}_x\text{Te}$  ( $0 \leq x \leq 1$ ) NWs by

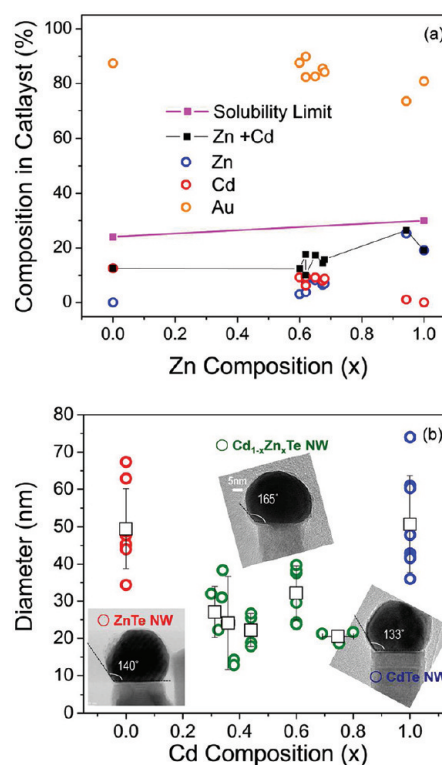


**Figure 3.** (a) Atomic composition of Cd (red circle), Zn (blue circle), Zn + Cd (black square), and Au (yellow circle) within the NW catalysts of various  $\text{Cd}_{1-x}\text{Zn}_x\text{Te}$  ( $0 \leq x \leq 1$ ) NWs, determined by the point energy dispersive X-ray by the convergent beam in TEM. The solubility limits (pink square and line) are estimated from the Au-Cd, Au-Zn phase diagram<sup>35</sup> at the growth temperature of  $500^\circ\text{C}$ . (b) Diameter variations of  $\text{Cd}_{1-x}\text{Zn}_x\text{Te}$  ( $0 \leq x \leq 1$ ) NWs as a function of Cd content were measured by transmission electron microscopy; ZnTe (red),  $\text{Cd}_{1-x}\text{Zn}_x\text{Te}$  (green), CdTe (blue). Three TEM images correspond to the representative ZnTe,  $\text{Cd}_{1-x}\text{Zn}_x\text{Te}$ , and CdTe NWs at each composition, showing the contact angle of catalysts on the NWs.

TEM probes, showing that both Zn and Cd contents vary below the equilibrium solubility limit. In fact, the total sum of the Zn and Cd content within the catalyst remains almost constant upon varying the Zn content. This suggests that the chemical potential ( $\mu_L$  and  $\mu_S$ ) variation,<sup>24</sup> and thus the  $\Delta\mu_{L-S}$ , upon the catalytic Cd-Zn alloying does not mark the difference between the ZB/WZ mixture formation of the parent compounds and the single ZB phase in the alloy. Instead, as adapted to Algra et al.<sup>6</sup> and Wallein et al.,<sup>22</sup> we attempted to trace the change in the liquid-vapor surface energy at the catalysts during the catalytic alloy growth by measuring the contact angles at the catalyst-NW interfaces, and equivalently the NW diameters as a function of Cd content, as in Figure 3b. Note that the lower L-V surface energy induces the higher contact angle, and the higher contact angle during the catalytic NW growth naturally yields the thinner NW, provided that the catalyst volume remains constant. It was found that upon the Cd:Zn alloying the NW diameter significantly decreases by a half on the average over the various Zn compositions from 50 to 25 nm. Equivalently, we also observed the noticeable increase of the contact angles from the

alloy NWs from  $130^\circ$  to  $140^\circ$  to  $165^\circ$ , as represented in the inserted TEM images. This strongly suggests that the surface energy is minimized during the catalytic alloying crystallization. Then the effectively reduced energy barrier for the nucleation predominantly favors the ZB phase. Thermodynamic calculations of the surface energy of binary liquid alloys by Butler's approach suggest that the surface energy is generally lowered below the linear interpolation between the two constituent parent elements.<sup>25</sup> Particularly, liquid Cd–Zn alloys have the positive heat of mixing,<sup>26</sup> and in the Cd–Zn alloy clusters a density functional theory calculation finds that the atomic binding energy of Cd–Zn is  $\sim 10$  meV, which is much smaller than those of Cd–Cd and Zn–Zn by severalfold.<sup>27</sup> The positive heat of mixing and the smaller binding energy in the Cd–Zn alloys suggest that the L–V surface energy is reduced by the Cd–Zn alloying. This is qualitatively consistent with our conclusions that the minimum surface energy during the catalytic alloying crystallization is responsible for the homogeneous ZB NW formation.

Thermodynamic stability of the single-crystalline ZB phase NW growth is further verified in an axially composition graded  $\text{Cd}_{1-x}\text{Zn}_x\text{Te}$  NW growth. We intentionally modulated the ZnTe and CdTe vapor pressures in the growth sequence by independently controlling the heating temperatures of ZnTe and CdTe powder precursors, i.e., by translating the position of CdTe powder-containing alumina boat from the heating zone. Figure 4a shows the representative TEM images of such a

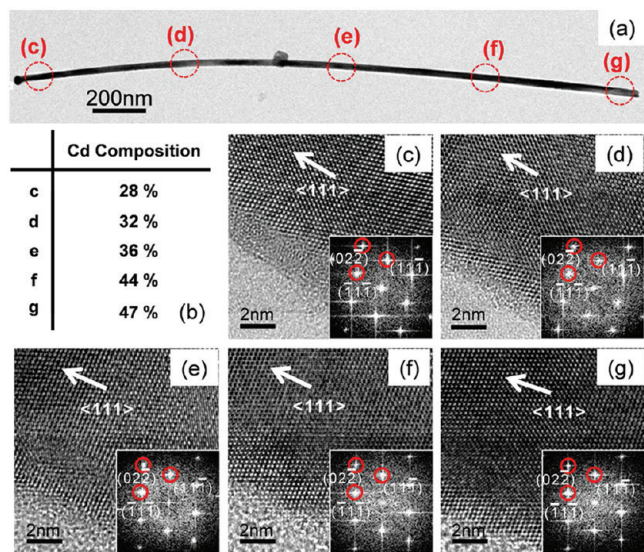


**Figure 4.** (a) Representative TEM images of an axially composition graded  $\text{Cd}_{1-x}\text{Zn}_x\text{Te}$  NW by changing relative vapor pressure of Cd and Zn precursors during the growth sequence. (b) The relative Cd composition measured from the EDX spectra collected from different position of  $\text{Cd}_{1-x}\text{Zn}_x\text{Te}$  NW along the axial direction. (c–g) High-resolution TEM images, marked with circles in (a) and corresponding fast Fourier transformation diffraction patterns, demonstrate that the SF-free ZB crystal structure is stably maintained along the  $\langle 111 \rangle$  growth direction over the on-NW composition gradation.

composition-graded  $\text{Cd}_{1-x}\text{Zn}_x\text{Te}$  NW. The axial variation in the relative composition of Zn and Cd is determined from the point energy dispersive X-ray by the convergent electron beam in TEM, and the result is summarized in Figure 4b. The high-resolution TEM images and diffraction patterns in Figure 4c–g, probed on different positions along the NW axis, demonstrated

that the NW are stacking fault free with the same crystal orientation along the entire NW length. This corroborates our observations that the catalytic alloying NW crystallization thermodynamically stabilizes the low-energy ZB phase NW growth over the broad range of the relative Cd:Zn compositions.

Figure 5a is the normalized photoluminescence (PL) spectra from  $\text{Cd}_{1-x}\text{Zn}_x\text{Te}$  ( $0 \leq x \leq 1$ ) NW arrays measured at 13 K,

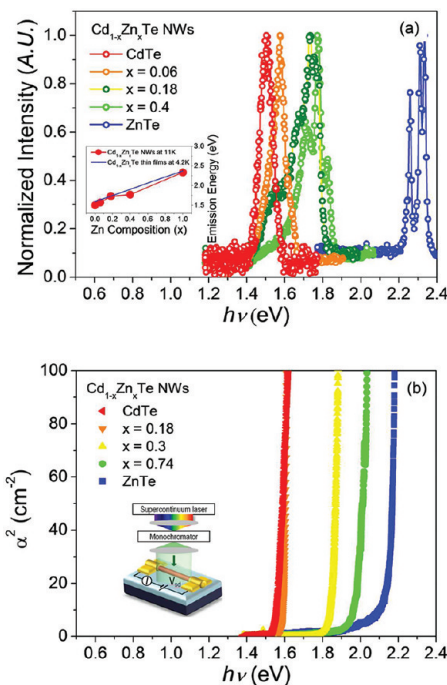


**Figure 5.** (a) Normalized photoluminescence (PL) spectra of  $\text{Cd}_{1-x}\text{Zn}_x\text{Te}$  ( $0 \leq x \leq 1$ ) NWs with different Zn compositions ( $x = 0, 0.06, 0.18, 0.4, 1$ ) at 13 K. The inset summarizes variation of band-gaps extracted from the main panel along with the known values of bulk  $\text{Cd}_{1-x}\text{Zn}_x\text{Te}$  crystals (b) Squared absorption coefficient spectra of  $\text{Cd}_{1-x}\text{Zn}_x\text{Te}$  ( $0 \leq x \leq 1$ ) NW photodetector as a function of incident photon energy. The inset shows normalized spectral responsivity of  $\text{Cd}_{1-x}\text{Zn}_x\text{Te}$  NWs measured at applied voltage 1.0 V across the NWs within 500–900 nm wavelengths by using broadband supercontinuum laser combined with a monochromator for the high-resolution spectra.

showing the gradual shift of the band-edge emission peaks from 521 nm (ZnTe NWs) to 825 nm (CdTe NWs) with decreasing Zn content. We often observed several multiple peaks, which can be assigned to the bound exciton states from Cd, Zn, and Te vacancies as commonly observed in CdTe, ZnTe, and  $\text{Cd}_{1-x}\text{Zn}_x\text{Te}$  thin films.<sup>28,29</sup> The band gap ( $E_g$ ) energy variation, determined from the PL peaks, is consistent with bulk alloys without any noticeable optical size effects. The spectral photocurrent of  $\text{Cd}_{1-x}\text{Zn}_x\text{Te}$  NWs was also collected as a function of Zn content near the fundamental band-gaps at room temperature as shown in Figure 5b. For this we have fabricated individual NW photodetectors on  $\text{SiO}_2(100 \text{ nm})/\text{p}^+\text{-SiO}_2$  wafers with the Ni(20 nm)/Au(150 nm) ohmic contacts via e-beam lithography and lift-off. Figure 5b shows the square of the absorption coefficient ( $\alpha^2$ ) as a function of incident photon energy, which is extracted from the photocurrent ( $I_{\text{ph}}$ ) responsivity in the inset by the relation  $I_{\text{ph}} \sim \exp(\alpha) \sim \exp(h\nu - E_g)^{1/2}$  for the direct gap transition. We found that the absorption edges of 1.46 and 2.23 eV for CdTe and ZnTe NWs and also verified that their shift with the Zn content variation is

consistent with those of bulk  $\text{Cd}_{1-x}\text{Zn}_x\text{Te}$  crystals (see also Figure S3). This finding, together with the PL peak shift, confirms that the appropriate Cd:Zn alloying can fully exploit the intrinsic energy band gap modulation in the full visible range.

Figure 6a is the time-resolved PL spectra of  $\text{Cd}_{1-x}\text{Zn}_x\text{Te}$  ( $0 \leq x \leq 1$ ) NWs, which was measured by using a mode-locked

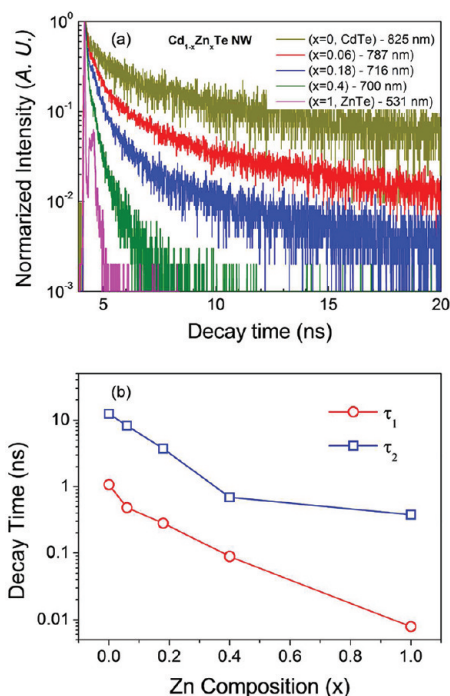


**Figure 6.** (a) Time-resolved photoluminescence (TRPL) spectra of  $\text{Cd}_{1-x}\text{Zn}_x\text{Te}$  ( $0 \leq x \leq 1$ ) NWs, measured at the near-band-edge by using a time-correlated single-photon counting system. (b) Decay time of the first ( $\tau_1$ , red) and the second ( $\tau_2$ , blue) components as a function of Zn content. TRPL spectra of all samples were fitted by a biexponential decay function.

(150 fs) Ti:sapphire laser system as an excitation source and a time-correlated single photon counting system for detection. The PL decays of all samples were fitted by a biexponential decay function, and the first ( $\tau_1$ ) and the second ( $\tau_2$ ) components of the decay times are plotted as a function of the Zn content in Figure 6b. We find in our  $\text{Cd}_{1-x}\text{Zn}_x\text{Te}$  NWs that both  $\tau_1$  and  $\tau_2$  continuously decrease with increasing Zn content. The slow decay time for the second component  $\tau_2$  is usually due to a nonsequential scattering caused by state blocking on the excited state,<sup>30</sup> and the measured  $\tau_1$  in our  $\text{Cd}_{1-x}\text{Zn}_x\text{Te}$  NWs may represent intrinsic carrier dynamics. It was reported that the carrier recombination velocity of ZnTe is 10 times faster than CdTe,<sup>31</sup> and the radiative lifetime of CdTe and ZnTe thin films is 18 ns and 150 ps.<sup>32,33</sup> Therefore, recalling that the SF in compound semiconductor NWs is known as nonradiative recombination centers,<sup>34</sup> we conclude that the carrier recombination lifetime is principally determined by the Cd:Zn alloying degree in the SF-free  $\text{Cd}_{1-x}\text{Zn}_x\text{Te}$  ( $0 \leq x \leq 1$ ) NWs.

## ■ ASSOCIATED CONTENT

### Supporting Information

Selected area diffraction patterns (SADP) and dark-field TEM images of ZnTe NWs, the full range XRD  $\theta$ - $2\theta$  scans of

$\text{Cd}_{1-x}\text{Zn}_x\text{Te}$  ( $0 \leq x \leq 1$ ) NWs, the chemical elemental analysis of the individual catalysts, and the absorption edge variation of  $\text{Cd}_{1-x}\text{Zn}_x\text{Te}$  NWs compared with bulk counterparts. This material is available free of charge via the Internet at <http://pubs.acs.org>.

## ■ AUTHOR INFORMATION

### Corresponding Author

\*E-mail: mhjo@postech.ac.kr.

### Author Contributions

<sup>†</sup>Equal contributors.

## ■ ACKNOWLEDGMENTS

This work was supported by Basic Science Research Program (2010-0017853 and 2010-0001873), Priority Research Centers Program (2010-0029711), Nano Original & Fundamental Technology R&D Program (2010-0019195), the MEST-AFOSR NBIT (No. K20716000006-07A0400-00610), and the WCU Program (R31-2008-000-10059-0) through the NRF funded by the MEST.

## ■ REFERENCES

- Hiruma, K.; Yazawa, M.; Katsuyama, T.; Ogawa, K.; Haraguchi, K.; Koguchi, M.; Kakibayashi, H. *J. Appl. Phys.* **1995**, *77*, 447.
- Johansson, J.; Karlsson, L. S.; Svensson, C. P. T.; Mårtensson, T.; Wacaser, B. A.; Deppert, K.; Samuelson, L.; Seifert, W. *Nature Mater.* **2006**, *5*, 574.
- Schroer, M. D.; Petta, J. R. *Nano Lett.* **2010**, *10*, 1618.
- Thelander, C.; Caroff, P.; Plissard, S.; Dey, A. W.; Dick, K. A. *Nano Lett.* **2011**, *11*, 2424.
- Woo, R. L.; Xiao, R.; Kobayashi, Y.; Gao, L.; Goel, N.; Hudait, M. K.; Mallouk, T. E.; Hicks, R. F. *Nano Lett.* **2008**, *8*, 4664.
- Algra, R. E.; Verheijen, M. A.; Borgström, M. T.; Feiner, L.-F.; Immink, G.; van Enckevort, W. J. P.; Vlieg, E.; Bakkers, E. P. A. M. *Nature* **2008**, *456*, 369.
- Bao, J.; Bell, D. C.; Capasso, F.; Wagner, J. B.; Mårtensson, T.; Trägårdh, J.; Samuelson, L. *Nano Lett.* **2008**, *8*, 836.
- Caroff, P.; Dick, K. A.; Johansson, J.; Messing, M. E.; Deppert, K.; Samuelson, L. *Nature Nanotechnol.* **2009**, *4*, 50.
- Dick, K. A.; Thelander, C.; Samuelson, L.; Caroff, P. *Nano Lett.* **2010**, *10*, 3494.
- Hao, Y.; Meng, G.; Wang, Z. L.; Ye, C.; Zhang, L. *Nano Lett.* **2006**, *6*, 1650.
- Johansson, J.; Karlsson, L. S.; Dick, K. A.; Bolinsson, J.; Wacaser, B. A.; Deppert, K.; Samuelson, L. *Cryst. Growth Des.* **2009**, *9*, 766.
- Joyce, H. J.; Wong-Leung, J.; Gao, Q.; Tan, H. H.; Jagadish, C. *Nano Lett.* **2010**, *10*, 908.
- Johansson, J.; Dick, K. A.; Caroff, P.; Messing, M. E.; Bolinsson, J.; Deppert, K.; Samuelson, L. *J. Phys. Chem. C* **2010**, *114*, 3837.
- Shtrikman, H.; Popovitz-Biro, R.; Kretinin, A.; Heiblum, M. *Nano Lett.* **2009**, *9*, 215.
- Shtrikman, H.; Popovitz-Biro, R.; Kretinin, A.; Houben, L.; Heiblum, M.; Bukala, M.; Galicka, M.; Buczek, R.; Kacman, P. *Nano Lett.* **2009**, *9*, 1506.
- Huang, H.; Ren, X.; Ye, X.; Guo, J.; Wang, Q.; Yang, Y.; Cai, S.; Huang, Y. *Nano Lett.* **2010**, *10*, 64.
- Chiaromonte, T.; Tizei, L. H. G.; Ugarte, D.; Cotta, M. A. *Nano Lett.* **2011**, *11*, 1934.
- Caroff, P.; Bolinsson, J.; Johansson, J. *IEEE J. Sel. Top. Quantum Electron.* **2011**, *17*, 829.
- Dick, K. A.; Caroff, P.; Bolinsson, J.; SMessing, M. E.; Johansson, J.; Deppert, K.; Wallenberg, L. R.; Samuelson, L. *Semicond. Sci. Technol.* **2010**, *25*, 024009.
- Woolley, J. C.; Ray, B. J. *Phys. Chem. Solids* **1960**, *13*, 151.
- Glas, F.; Harmand, J. C.; Patriarche, G. *Phys. Rev. Lett.* **2007**, *99*, 146101.

- (22) Wallentin, J.; Ek, M.; Wallenberg, L. R.; Samuelson, L.; Deppert, K.; Borgström, M. T. *Nano Lett.* **2010**, *10*, 4807.
- (23) Algra, R. E.; Verheijen, M. A.; Feiner, L.; Immink, G. G. W.; van Enckevort, W. J. P.; Vlieg, E.; Bakkers, E. P. A. M. *Nano Lett.* **2011**, *11*, 1259.
- (24) Garrard, B. J.; Wanklyn, B. M.; Lipko, H. A. J. *Cryst. Growth* **1981**, *53*, 297.
- (25) Bhatia, A. B.; March, N. H. *J. Chem. Phys.* **1978**, *68*, 4651.
- (26) Dutkiewicz, J.; Zakulski, W. *Bull. Alloy Phase Diagrams* **1984**, *5*, 30.
- (27) Erkoç, Ş. *Chem. Phys. Lett.* **2003**, *369*, 605.
- (28) Stadler, W.; Hofmann, D. M.; Alt, H. C.; Muschik, T.; Meyer, B. K.; Weigel, E.; Müller-Vogt, G.; Salk, M.; Rupp, E.; Benz, K. W. *Phys. Rev. B* **1995**, *51*, 10619.
- (29) Carvalho, A.; Tagantsev, A. K.; Oberg, S.; Briddon, P. R.; Setter, N. *Phys. Rev. B* **2010**, *81*, 075215.
- (30) Buckle, P. D.; Dawson, P.; Hall, S. A.; Chen, X.; Steer, M. J.; Mowbray, D. J.; Skolnick, M. S.; Hopkinson, M. J. *Appl. Phys.* **1999**, *86*, 2555.
- (31) Bose, D. N.; Ahrenkiel, R. K.; Bhunia, S. J. *Appl. Phys.* **1999**, *86*, 6599.
- (32) Dai, D. C.; Monkman, A. P. *Phys. Rev. B* **2011**, *84*, 115206.
- (33) Wuister, S. F.; Donega, C.; Meijerink, A. J. *Chem. Phys.* **2004**, *108*, 17393.
- (34) Parkinson, P.; Joyce, H. J.; Gao, Q.; Tan, H. H.; Zhang, X.; Zou, J.; Jagadish, C.; Herz, L. M.; Johnston, M. B. *Nano Lett.* **2009**, *9*, 3349.
- (35) *Binary Alloy Phase Diagram*, 2nd ed.; ASM International: Materials Park, OH, 1990.